INT. J. NUM. METH. HEAT FLUID FLOW, VOL. 6, 3–18 (1996)

NUMERICAL STUDY OF GREY-BODY SURFACE RADIATION COUPLED WITH FLUID FLOW FOR GENERAL GEOMETRIES USING A FINITE VOLUME MULTIGRID SOLVER

L. KADINSKI AND M. PERIĆ

Lehrstuhl für Strömungsmechanik, University of Erlangen-Nürnberg, Cauerstr. 4, D-91058, Erlangen, Germany

ABSTRACT

The paper presents a numerical technique for the simulation of the effects of grey-diffusive surface radiation on fluid flow using a finite volume procedure for two-dimensional (plane and axi-symmetric) geometries. The governing equations are solved sequentially, and the non-linearities and coupling of variables are accounted for through outer iterations (coefficients updates). In order to reduce the number of outer iterations, a multigrid algorithm was implemented.

The radiating surface model assumes a non-participating medium, semi-transparent walls and constant elementary surface temperature and radiation fluxes. The calculation of view factors is based on the analytical evaluation for the plane geometry and numerical integration for axi-symmetric geometry. A shadowing algorithm was implemented for the calculation of view factors in general geometries.

The method for the calculation of view factors was first tested by comparison with available analytical solutions for a complex geometric configuration. The flow prediction code combined with radiation heat transfer was verified by comparisons with analytical one-dimensional solutions. Further test calculations were done for the flow and heat transfer in a cavity with a radiating submerged body. As an example of the capabilities of the method, transport processes in metalorganic chemical vapour deposition (MOCVD) reactors were simulated.

KEY WORDS Grey-body radiation Finite volume Multigrid Subsonic flow CVD

INTRODUCTION

In many problems of engineering interest radiative heat transfer plays an important role and it becomes especially important in high-temperature systems. In some applications, such as conventional boilers and furnaces, combustion, nuclear fission and fusion, etc., the medium can absorb, emitt and scatter the energy. For a review of the recent advances in this area see Reference 1. In other types of problems, when the media are not radiatively participating, only radiation exchange among surfaces should be taken into account. This classical problem is relatively simple and well understood. References 2, 3 discuss radiation phenomena in great detail and present required theory, formulae and methods for general cases and some applications. References 4–8 consider the radiation heat transfer in the Czochralski crystal growth. In References 9–13 the effects of wall radiation in crystal growth by MOCVD (Metalorganic chemical vapour deposition) method were studied.

The modelling equations in all the mentioned publications are solved by using single grid methods. Due to excessive computing times, the calculations were limited to relatively coarse grids and the distinction between the errors due to discretization and those due to the modelling

0961–5539/96/030003–16$2.00

Received November 1993
Revised March 1994

of the physical processes was not possible. In recent years, multigrid finite difference (FD) and finite volume (FV) methods applicable to the solution of coupled, non-linear differential equations have been developed (see References 14 and 15 for MOCVD modelling). The application of the multigrid idea results in an approximately linear increase of computing time with grid refinement, allowing much finer grids to be used and, therefore, more accurate solutions to be obtained.

In this paper, a multigrid finite volume solution procedure is employed to predict the non-participating flows and heat transfer in complicated two-dimensional (2-D) geometries when the boundary surfaces are considered to be radiating, grey-diffusive and semi-transparent. By systematically refining the grids, it was possible to evaluate the discretization errors and make sure that they were negligibly small on finest grid. Due to the multigrid solution procedure, computing times were reduced by an order of magnitude or more in comparison with standard methods.

The algorithm for the calculation of view factors was tested by comparison with analytical expressions for a complex geometry configuration. The flow prediction code combined with radiation heat transfer was verified by comparisons with analytical one-dimensional (1-D) solutions. Further test calculations were done for the flow and heat transfer in a cavity with a radiating submerged body. Finally, simulations of flow and radiation heat transfer in horizontal and vertical MOCVD reactors were performed.

MODELLING EQUATIONS

Flow model equations

The gas flows with very low Mach numbers and large temperature differences are considered. These flows can be described by the conservation laws for mass, momentum and energy, expressed in a coordinate-free form as follows,

$$\frac{\partial \rho}{\partial t} + \nabla \cdot (\rho \vec{V}) = 0, \tag{1}$$

$$\frac{\partial (\rho \vec{V})}{\partial t} + \nabla \cdot (\rho \vec{V} \vec{V}) = -\nabla p + \rho \vec{g} + 2\nabla \cdot (\mu \dot{S}) - \frac{2}{3} \nabla (\mu \nabla \cdot \vec{V}), \tag{2}$$

$$\frac{\partial (\rho c_p T)}{\partial t} + \nabla \cdot (\rho \vec{V} c_p T) = \nabla \cdot (\lambda \nabla T), \tag{3}$$

where $\vec{V}$ is the velocity vector, T is the temperature, p is the pressure, $\dot{S}$ is the deformation rate tensor, $\vec{g}$ is the gravitational acceleration vector, and c_p is the specific heat at constant pressure. The deformation rate tensor $\dot{S}$ is defined as: $\dot{S} = \frac{1}{2}[\nabla \vec{V} + \nabla \vec{V}^T]$. The dynamic viscosity, μ, thermal conductivity, λ, and density, ρ, of the gas are functions of temperature,

$$\mu = \mu(T), \qquad \lambda = \lambda(T), \qquad \rho = \rho(T), \qquad P_0 = \rho R T. \tag{4}$$

In the equation of state, P_0 is the constant characteristic pressure and R is the gas constant.

Boundary conditions

The transport equations (1)–(3) have to be supplemented with appropriate boundary conditions on all boundary surfaces of the solution domain, such as walls, symmetry planes or lines, inflow and outflow. The boundary conditions for the momentum equations include a specified velocity profile at the inlet, zero velocities on solid walls (no slip and no penetration), and zero velocity gradients at the outlet ("soft" boundary conditions). For the energy transport equation, a special analysis is required to determine the boundary conditions at non-isothermal walls. At the inlet, the temperature profile is prescribed. At the outlet and symmetry boundaries, zero temperature gradient is assumed.

Enclosures with semi-transparent grey-diffusive radiating walls and non-participating gas inside and ambient outside are considered. In this case the energy flux to the inside wall is composed of two contributions: radiative transfer from surfaces facing the wall and conduction by the gas. Energy is lost from the wall to the ambient by radiation and cooling by the surrounding (ambient) gas. Thus, the wall boundary conditions take the form,

$$\text{Ambient-Wall:} \quad -\left(\lambda\frac{\partial T}{\partial n}\right)_w^{out} = h(T_w^{out}-T_a)-q_i^{out}+q_o^{out} \tag{5}$$

$$\text{Gas-Wall:} \quad T_w^{in}=T_g, \qquad \left(\lambda\frac{\partial T}{\partial n}\right)_w^{in}=\left(\lambda\frac{\partial T}{\partial n}\right)_g-q_i^{in}+q_o^{in} \tag{6}$$

where the indices "w" and "g" are related to the wall and to the gas, respectively, T_a is the temperature of the ambient, h is the overall heat transfer coefficient given by heat transfer correlation, q^{out} and q^{in} are the radiation fluxes to the wall (index i) and from the wall (index o) on the outer and inner side, respectively, and $\partial/\partial n$ is the derivative normal to the wall. In the case of thin walls, the boundary conditions could be simplified by assuming a constant temperature gradient across the wall. While this approximation makes little difference to the complexity of the wall energy balance, it simplifies the radiation analysis in the case of semi-transparent walls. (If the walls are thick enough, the processes of conduction and radiation transfer in the walls should be taken into account.) Under this assumption, and by neglecting the temperature difference between both sides of the wall ($T_w^{in}\approx T_w^{out}$), the energy boundary condition at the wall takes the form,

$$-\lambda\left(\frac{\partial T}{\partial n}\right)_g = h(T-T_a)-(q_i^{out}-q_o^{out}+q_i^{in}-q_o^{in})^{q_{net}} \tag{7}$$

where T is the temperature of the gas on the inner side of the wall. To close the model equations, the radiation fluxes have to be specified.

Radiation model equations

The radiation fluxes for the elementary wall surface element k ($k=1, \ldots, N$, where N is the total number of elementary surfaces on the wall) can be calculated using Stefan–Boltzmann equation and definitions of emissivity (E), reflectivity (R), and transmissivity (Tr) as follows[2,3],

$$q_{i,k}^{in}=\sum_{j=1}^{N} q_{o,j}^{in}F_{kj}, \tag{8}$$

$$q_{o,k}^{in}=\sigma E_k T_k^4+R_k q_{i,k}^{in}+\sigma Tr_k T_a^4, \tag{9}$$

$$q_{i,k}^{out}=\sigma T_a^4, \tag{10}$$

$$q_{o,k}^{out}=\sigma E_k T_k^4+R_k q_{i,k}^{out}+Tr_k q_{i,k}^{in}, \tag{11}$$

where σ is the Stefan–Boltzmann constant and F_{kj} are the view factors. The major assumptions in deriving these equations, which limit their validity, are grey-diffusive surfaces and uniform temperatures for each radiating surface k. Without introducing uniform temperature surfaces, in (8) surface integrals would appear instead of view factors. If radiative properties are wavelength depending, (8)–(11) should be written in differential form. In this case some simplification should be done in order to get a closed form of (8)–(11), for instance, using the band model (see e.g. Reference 3 for the theory and Reference 12 where two-band model was used to approximate optical properties of quartz).

After summation of fluxes and using relation $E+R+Tr=1$, the net radiation flux q_{net} for the kth surface element becomes (cf. (7)),

$$q_{net,k}=E_k(q_{i,k}^{in}-2\sigma T_k^4+\sigma T_a^4), \tag{12}$$

where $q_{i,k}^{in}$ is defined by the system of equations (8)–(9), providing the heat exchange relationship between the radiation boundaries. Thus the heat transfer in the gas and between the walls is coupled through (7), since the temperature of the gas at the wall is equal to the wall temperature. If the jth surface is an opening (inflow or outflow), the radiation flux in (8) is calculated as,

$$q_{j,k}^{in} = \sigma T_a^4 \tag{13}$$

and no special modifications for the system (8)–(9) are required as it was done in Reference 16. Since the medium is transparent, the gas temperature at the openings is not affected by the radiation. The system (8)–(9) can be resolved once the view factors are known.

NUMERICAL SOLUTION METHOD

The mathematical model described above was implemented in a solution procedure for two-dimensional (plane or axi-symmetric) laminar flows described by Demirdžić and Perić[17] and Durst *et al.*[15]. For this reason, only a short description of the solution procedure is given and only the new features associated with radiation heat transfer are described in detail.

Discretization method

The equations (1)–(3) are discretized on non-orthogonal grids using a finite volume approach with collocated arrangement of variables. Central differences (2nd order) are used to approximate both convection and diffusion fluxes through control volume (CV) faces. In the momentum equations, the pressure and gravitational forces are treated as source terms. The specific source is evaluated at the center of the CV, and treated as a mean value over the whole CV. The boundary conditions are incorporated in the solution procedure either by specifying the CV face fluxes or calculating them from their discretized expressions using specified boundary values or gradients of the variables.

In (7)–(9), the boundary CV faces are treated as the elementary surfaces with temperature T_k. The main assumption in this formulation is that each CV face at the boundary is a radiation surface which has constant properties; namely, those associated with cell face center (boundary nodes). The discretized boundary conditions (7) couple the discretized energy equation (3) with the non-linear system (8)–(9), and the temperature of every node on the boundary is coupled with every other node on the boundary. If this matrix system is solved as a coupled system (after some linearization of (8)–(9)), the computing cost increases significantly, because effective solvers for diagonal matrices can not be applied. An alternative is a decoupled iterative approach, in which the linear system (8)–(9) is solved for given boundary temperatures, and then the resultant heat fluxes are used as specified boundary fluxes[16].

The solution of the resulting coupled set of algebraic equations for the momentum transport is based on the SIMPLE algorithm[18]. The momentum equations are assembled by treating pressure, mass fluxes, and other variables as known (values from previous iteration are used) and the resulting linear systems are solved by applying one iteration of the Strongly Implicit Procedure (SIP) of Stone[19]. With these intermediate velocities, which do not satisfy the continuity equation (1), new mass fluxes are calculated, whose imbalance provides the source term for the pressure correction equation. It is solved by applying up to 10 iterations of the SIP-solver (inner iterations). The pressure correction is used to correct velocities, pressure and mass fluxes, which then satisfy the continuity requirement. Thereafter, the system (8)–(9) is solved in order to provide boundary fluxes needed for the temperature equation.

The finite-volume approximation of the boundary condition (7) leads to non-linear equation for the boundary temperature. It was found that simple linearization of (7),

$$-\lambda \left.\frac{\partial T^{new}}{\partial n}\right|_k = (T_k^{new} - T_a)[h + 2\sigma E_k (T_k^n + T_a)((T_k^n)^2 + T_a^2)] - E_k(q_{i,k}^{in} - \sigma T_a^4) \tag{14}$$

where T^n is the temperature from the previous iteration and T^{new} is the new approximation for the boundary temperature, in some cases leads to divergence. Instead of that, (7) for every boundary node is iterated until convergence. Thereafter, the temperature equation is assembled and relaxed by applying one SIP iteration. The new density is then calculated from the equation of state (4). Based on these velocity and temperature fields, the coefficients of the difference equations are updated, and a new outer iteration is started. The process is repeated until convergence.

In all calculations, also for the system (8)–(9), the under-relaxation is used in order to ensure the convergence of the procedure,

$$q^{n+1}=\alpha q_*^{n+1}+(1-\alpha)q^n, \tag{15}$$

where α is the under-relaxation parameter, $0\leqslant\alpha\leqslant 1$, q^{n+1} is the final solution, q_*^{n+1} is the intermediate solution, and q^n is the solution from the previous iteration. In most of the simulations presented in this paper a relaxation parameter between 0.8 and 1.0 was employed for the system (8)–(9). No special study was done to determine an optimal set of parameters.

The convergence criterion used here is the requirement that the sum of abolute residuals in all equations, normalized by a characteristic value for each equation, falls seven orders of magnitude, which guarantees that the iterative convergence errors are negligibly small (less than 0.001%).

Multigrid solver

The rate of convergence of the above solution method is highest at the beginning of the iteration process. It becomes worse after a few outer iterations, an effect being more pronounced as the grid is refined. In order to speed up the convergence of the outer iterations, the multigrid procedure based on the Full Approximation Scheme (FAS) for non-linear coupled equation systems is used[14]. Details of the described algorithm can be found in References 14 and 20.

In the present implementation, the gain flux q_{net} is calculated on coarse grid by summing the fine grid fluxes and used in (7) without recalculating. At the current finest grid (7) is used together with the system (8)–(9) as it was described for the single grid algorithm. The cost of obtaining the coarser grid solutions is compensated by having a good initial approximation for all variables on the next finer grid.

The systematic grid refinement used in the multigrid algorithm to achieve higher convergence rates facilitates also the evaluation of discretization errors. These are proportional to the grid spacing and the order of the discretization scheme[21]. For sufficiently fine grids and second order discretization (as used in this study), the discretization errors on the finer grid are about one third of the difference in solutions between that and the next coarser grid.

View factor calculations

The analysis of radiation interchange among diffusively emitting and reflecting surfaces depends on the knowledge of view factors. For two black bodies the view factor is defined as the fraction of radiation energy leaving the surface i that arrives at the surface j (see, e.g. References 2, 3)

$$F_{ij}=\frac{1}{A_i}\int_{A_i}\int_{A_j}\frac{\cos\theta_i\cos\theta_j}{\pi r_{ij}^2}\,\mathrm{d}A_i\,\mathrm{d}A_j \tag{16}$$

where A_i and A_j are the areas of surfaces i and j respectively, and θ_i and θ_j are the angles between the normal vectors to surfaces and the connecting line with a length r_{ij} (see *Figure 1*). Some useful correlations can be derived from (16) and the energy conservation principle,

Reciprocity

$$A_iF_{ij}=A_jF_{ji} \tag{17}$$

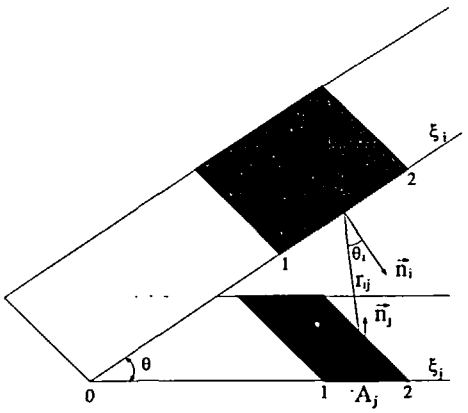

Figure 1 On the definition of view factors

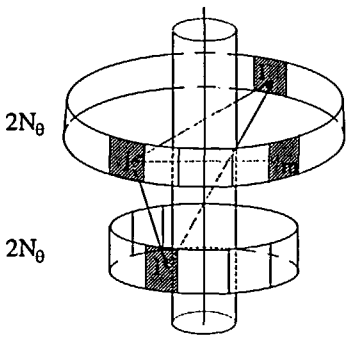

Figure 2 On the numerical evaluation of view factors in axi-symmetric geometries ($F_{ji}=0; F_{il}=0; F_{jm}\neq 0; F_{ji}\neq 0$)

Summation ($A_{12}=A_1\cup A_2$, $A_{34}=A_3\cup A_4$)

$$(A_1+A_2)F_{1\cup 23\cup 4}=A_1(F_{13}+F_{14})+A_2(F_{23}+F_{24}) \tag{18}$$

Conservation

$$\sum_{j=1}^{N} F_{kj}=1 \tag{19}$$

where N is the total number of boundary cell faces.

Despite of the flow and radiation problem being considered as 2D, the view factor problem is three-dimensional. Two different strategies for the calculation of the view factors, depending on the geometry, are presented below.

Plane geometry

For the plane geometries the view factor between two elementary surfaces is the factor between two infinite stripes and, therefore, can be evaluated analytically (see *Figure 1*),

$$F_{ji}=\frac{\xi_{i,2}-\xi_{i,1}}{2(\xi_{j,2}-\xi_{j,1})}\left[\frac{\xi_{i,2}+\xi_{i,1}-2\xi_{j,1}\cos\theta}{\sqrt{d^2+\xi_{j,1}^2+\xi_{i,2}^2-2\xi_{j,1}\xi_{i,2}\cos\theta}+\sqrt{d^2+\xi_{j,1}^2+\xi_{i,1}^2-2\xi_{j,1}\xi_{i,1}\cos\theta}}\right.$$
$$\left.-\frac{\xi_{i,2}+\xi_{i,1}-2\xi_{j,2}\cos\theta}{\sqrt{d^2+\xi_{j,2}^2+\xi_{i,2}^2-2\xi_{j,2}\xi_{i,2}\cos\theta}+\sqrt{d^2+\xi_{j,2}^2+\xi_{i,1}^2-2\xi_{j,2}\xi_{i,1}\cos\theta}}\right]\phi. \tag{20}$$

where d is the distance between two parallel stripes ($\theta=0$) and $d=0$ when stripes are not parallel ($\theta\neq 0$), and ξ_i and ξ_j are the coordinates measured from the crossing point of the lines passing along the two surfaces, cf. *Figure 1*.

Axi-symmetric geometry

For the axi-symmetric geometries there is no closed form for the view factor evaluation. One possibility is an analysis of the concrete geometrical configuration and using the analytical formulas (see, e.g. Reference 4 for Czochralski problem). Compared to the numerical evaluation this approach is significantly faster, but it only works if the closed form exists and can not be applied for arbitrary geometry.

In this study the numerical evaluation is employed. The algorithm operates by discretizing azimuthally each surface element into $2N_\theta$ facets as it is shown in *Figure 2*. The view factor between two surface elements can be found as the sum of view factors between a pair of facets using view factor algebra correlations (17)–(18) and symmetry,

$$A_i F_{ik} = 4N_\theta \sum_{m=n}^{N_\theta+n} \delta_m A_n F_{nm}, \tag{21}$$

where $\delta_m = 1$, $m = n+1, \ldots, n+N_\theta-1$;; $\delta_m = 0.5$, if $m = n$, $n+N_\theta$, and n is any number between 1 and N_θ.

Each pair of facets is taken to be either totally visible to each other or to be totally shadowed by the obstacles crossing the line connecting the centroids of these two facets. If the facets can see each other, then the algorithm calculates the view factor between them as,

$$A_i F_{ik} \approx 4N_\theta \sum_{m=n}^{N_\theta+n} \delta_m \frac{\cos\theta_n \cos\theta_m}{\pi r_{nm}^2} A_n A_m. \tag{22}$$

Taking into account the correlations between the elementary surface areas, the numerical approximation for the view factor becomes,

$$F_{ik} \approx \frac{A_k}{\pi N_\theta} \sum_{m=n}^{N_\theta+n} \delta_m \frac{\cos\theta_n \cos\theta_m}{r_{nm}^2}. \tag{23}$$

In order to get better approximation for the numerical evaluation of the view factor, one modification was done: each elementary surface can be discretized not only azimuthally but also radially or/and axially into N_i and N_k elementary subsurfaces. In this case the nth elementary surface consists of N_n elementary subsurfaces and the numerical approximation for the view factor becomes,

$$F_{ik} = \frac{1}{A_i} \sum_{i_m=1}^{N_i} A_i^m \sum_{k_l=1}^{N_k} F_{i_m k_l}, \tag{24}$$

where $F_{i_m k_l}$ is given by (23). ((24) itself is exact.) In this case the computational cost increases by $N_i N_k$ times.

After computing the view factors for the finest grid, the view factors for all other coarse grids can be recursively calculated using (24), because every boundary surface on the grid $k-1$ consists of two corresponding surfaces on the grid k.

The major complication with the view factor calculation is the possibility of partial blocking or shadowing between two surfaces by an intervening body or obstacle or by another boundary surface, as illustrated in *Figure 2*. The present shadowing algorithm is based on the blockage of lines connecting centroids of separate surfaces.

After the testing of the algorithm it was found that the main error occurs in the computation for the neighbouring surfaces. In order to improve the results, the following semi-empirical correction technique was employed.

Let F_{in} be the maximal view factor for given index i: $F_{in} = \max_{j=1,N} F_{ij}$. The corrected view factor is defined as follows,

$$F_{in}^{corr} = 1 - \sum_{j, j\neq n}^{N} F_{ij}, \tag{25}$$

if $n > i$, or no correction, if $n < i$. After correction, the change of error for the index n is checked. If the error has not increased, the correction is adopted. This technique is self-consistent, because the change of F_{in} involves the change of F_{ni} due to the reciprocity correlation (19). It was tested by comparison of the corrected view factors with the analytical expressions. The corrected values were found to be sufficiently accurate.

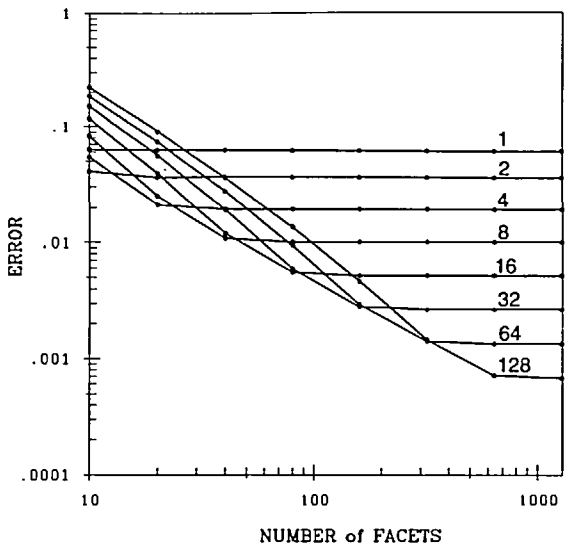

Figure 3 Error in view factor calculation defined by equation (26) for the confirugation C-72 as a function of azimuthal discretization. Curve numbers denote number of subsurfaces N_{sub} in radial and axial direction

Verification of the view factor calculation algorithm

The accuracy of the calculated view factors was examined by comparison with the exact expressions. A great number of analytically calculated view factors for various geometries can be found in Reference 22. Here the results for the test case C-72 (outer surface of cylinder to annular disk at the end of cylinder, cylinder length $L=1$, radius $R=1/2$) are presented in *Figure 3*. The error was defined as follows,

$$e=|F_{12}^{num}-F_{12}^{anal}|. \tag{26}$$

The error is more sensitive to the axial/radial than to the azimuthal discretization, and inverse proportional to the number of subsurfaces N_{sub}. This is in accordance with the order of integration scheme. The error is not sensitive to the azimuthal discretization for $N_\theta > N_\theta^0$, where N_θ^0 is a definite number, depending on the configuration. The results of calculations give a criteria for the choice of parameters N_θ and N_{sub} for the needed accuracy. As was mentioned above, the main error occurs in the computation for the neighbouring surfaces. Therefore, the contribution of that error is greater for smaller N_θ, as is demonstrated in the *Figure 3*.

It was found that the computational time was asymptotically proportional to the number of all elementary surfaces: $t \sim c \cdot N_\theta \cdot N_{sub}^2$, where c is configuration dependent. For the case C-72, $c=3.9\times10^{-5}$ s. (All calculations were carried out on a SUN SPARC 1+ workstation with approx. 1.5 MFlops performance.)

Another measure of the accuracy of the computations is the sum of view factors. According to (19), for each elementary surface in an enclosure the sum of view factors referring to other elements is equal unity. Therefore, the error can be defined as,

$$e_C=\max_{k=1,N}\left|1-\sum_{j=1}^{N}F_{kj}\right| \quad \text{or} \quad e_L=\frac{1}{N}\left(\sum_{i=1}^{N}\left(1-\sum_{j=1}^{N}F_{kj}\right)^2\right)^{1/2} \tag{27}$$

The second test example was taken from Reference 4—the accuracy of the view factor computations for two closed, concentric circular cylinders for the grid with 16×16 CV (N=64)

Table 1 Errors in view factor calculations for two concentric circular cylinders (cf. (27))

		without correction		after correction	
N_θ	N_{sub}	e_C	e_L	e_C	e_L
100	4	0.09	2.95×10^{-3}	0.018	7.30×10^{-4}
	8	0.05	1.27×10^{-3}	0.007	2.12×10^{-4}
200	4	0.09	2.27×10^{-3}	0.009	3.79×10^{-4}
	8	0.02	5.37×10^{-4}	0.004	1.63×10^{-4}

was examined. The results of calculations with and without the correction technique described by (25) are summarized in *Table 1.*

The results of calculations agree well with the first test case and show that, in order to achieve the reference accuracy for the grid of 16×16 CV, the elementary surfaces should be subdivided into 4–8 subsurfaces. This means, that view factor calculations for the grid of 64×64 CV and of 128×128 CV do not need further subdivision of CV faces into subsurfaces. Because the algorithm is intended for very find grids, the applied integration technique is sufficiently accurate.

RESULTS OF APPLICATION

The aim of the present study was to develop a numerical solution procedure which gives accurate predictions of the effects of grey-diffusive surface radiation on the fluid flow. To test the implementation described in the previous sections, several model problems were solved.

The efficiency and numerical accuracy of the base method for flow prediction has been proven elsewhere[14,15,20,21]. Attention is here focussed only onto extensions concerning the effects of radiation heat transfer.

Validation of the numerical method

First a simple problem with a 1D analytical solution was chosen. The enclosure consisting of two infinite parallel plates of length L at a distance H is considered, with $H/L\ll1$. The two plate surfaces are grey and have radiating properties E_1, R_1, Tr_1 and E_2, R_2, Tr_2, respectively. The first surface is kept at a constant temperature $T_1=T_0$, and for the second surface, the boundary conditions (7), (12) are supposed.

The heat conduction equation $d^2T(y)/dy^2=0$ has the solution $T(y)=ay+T_0$, where a is an unknown constant. The solution satisfies the boundary condition (cf. (7), (12)),

$$-\lambda a=h(T_2-T_a)-q^{(2)}_{nel}(a). \tag{28}$$

The gain radiative heat flux can be calculated analytically using symmetry and one-dimensionality as follows (cf. (8)–(9)),

$$q^{(2)}_{nel}=\frac{E_2\sigma}{1-R_1R_2}\left[T_2^4(R_1E_2-2+2R_1R_2)+T_1^4E_1+T_a^4(R_1Tr_2+Tr_1+1-R_1R_2)\right], \tag{29}$$

where $T_2=aH+T_0$. Equation (28) is the non-linear equation for the constant a and can be resolved, e.g. by the Newton iterations method. One numerical test was done for $\lambda=0.196$, $H=2\times10^{-2}$, $T_0=900$, $h=0$, and $\varepsilon_1=\varepsilon_2=\varepsilon$. The temperature of the second plate was compared with a 2D solution for the same set of constants. Similar expressions can be derived for an axi-symmetric geometry, where the enclosure consists of two infinite coaxial cylinders. In this case the solution is $T(r)=a\ln((r+r_0)/r_0)+T_0$ and the gain net flux can also be calculated analytically. The comparison of analytical solutions and results of calculations for the temperature

Table 2 Comparisons of analytical and numerical solutions for the temperature T_2 in plane and axi-symmetric geometries

	T_2, plane		T_2, axi-symmetric	
ε	analytical	numerical	analytical	numerical
0.1	779.17	779.0	704.80	696.0
0.5	740.36	740.0	676.30	674.0
0.9	758.46	758.0	688.78	688.0

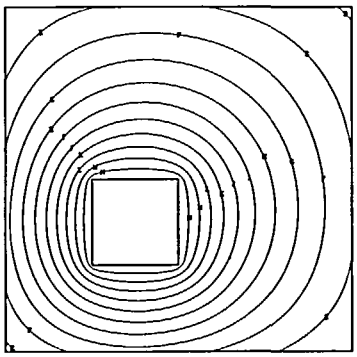

Figure 4 (a) Isotherms for the cavity with a radiating obstacle—pure heat transfer; contour levels from 950 K (N) to 450 K (D), in steps of 50 K

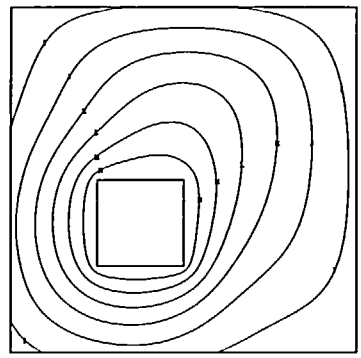

Figure 4 (a) Isotherms for the cavity with a radiating obstacle—pure heat transfer; contour levels from 950 K (N) to 450 K (D), in steps of 50 K

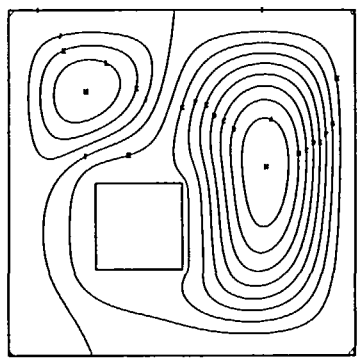

Figure 4 (c) Streamlines for the cavity with a radiating obstacle—flow and heat transfer. $\Psi_{max} = 2.2 \times 10^{-5}$ (M), $\Psi_{min} = -6.5 \times 10^{-5}$ (N)

of the second surface are shown in *Table 2*. In the calculations the aspect ratio for the plane case was 0.01 and for the axi-symmetric case 0.05. The discrepancies in the results are greater for the axi-symmetric case than for the planar case, the main source of the error being the finite size of plates.

Flow and heat transfer in a cavity

The purpose of this example is to evaluate the efficiency and the accuracy of the suggested method. The buoyancy-driven flow in a square cavity with a radiating square submerged body

Table 3 Errors in view factor calculations for the square cavity with a radiating obstacle

Grid	Error	
	e_C	e_L
8×8	0.113	1.13×10^{-2}
16×16	0.056	4.32×10^{-3}
32×32	0.028	1.56×10^{-3}
64×64	0.014	5.47×10^{-4}
128×128	0.007	2.58×10^{-4}

is considered. The temperature of the body is $T_0=1000$ K and the ambient temperature is $T_a=300$ K. At all cavity walls the boundary conditions are assumed ($h=0$ for flow and heat transfer, and $h=30$ for pure heat transfer). All transport properties were chosen for hydrogen at the normal atmospheric pressure: $P_0=1$ bar. The length of the cavity side wall is $H=10$ cm, and the size of radiation body is 2.5 cm. The upper right corner of the radiating body is in the centre of the cavity, cf. *Figure 4*. The resulting characteristic dimensionless numbers are,

$$Ra=\frac{g\rho_{ref}^2H^3(T_0-T_a)}{\mu_{ref}^2T_{ref}}Pr=4.632\times10^4 \quad \text{and} \quad \text{Rad}=\frac{\sigma T_0^3H}{\lambda_0}=3.126\times10^1 \tag{30}$$

Reference values were defined for the reference temperature: $T_{ref}=\frac{1}{2}(T_0+T_a)$. The finest grid had 128×128 CV and five grid levels. The coarse grids were subsets of the finer grids.

All view factors had to be calculated using shadowing option. In order to check the accuracy of the algorithm, the view factors were calculated on all five grids independently. The errors of the calculations are given in *Table 3*. They show that the required accuracy can be achieved by subdividing the boundary elements and that for sufficiently fine grids the additional subdivision is not needed.

In order to investigate the efficiency of the multigrid algorithm, the calculations were done using both multigrid and single grid methods. The results showed that for this moderately fine grid of 128×128 CV the multigrid method is 30–50 times faster than the single grid version. This finding is in accordance with speed-up factors found for problems without radiation heat transfer, cf. Reference 14.

The results for pure heat transfer and flow and heat transfer are shown in *Figure 4*. The effect of fluid flow on heat transfer is obvious from the comparison of isotherms for the case of pure heat transfer (*Figure 4a*) and heat transfer with fluid flow (*Figure 4b*). In addition to radiation and conduction, the heat is now transported by convection in the flow direction, as shown by streamlines (*Figure 4c*).

The numerical accuracy of these results is assessed by comparing the solutions on subsequent grids. From visual comparison no difference in flow and isotherm pattern between the finest grids could be observed. Comparison of some integral parameters (total heat flux through obstacle walls, strength of the eddies) showed monotonic convergence towards grid independent values with the difference between solution on two finest grids of the order of 0.3%. This implies that the discretization error on the finest grid is of the order of 0.1%. Variation in total heat flux through one of the obstacle walls with grid refinement is shown in *Figure 5*.

Flow in MOCVD reactors

MOCVD has become an established technique for growing thin, high purity, epitaxial films of compound semiconductors for modern optoelectronic applications like solar cells, lasers and high electron mobility transistors.

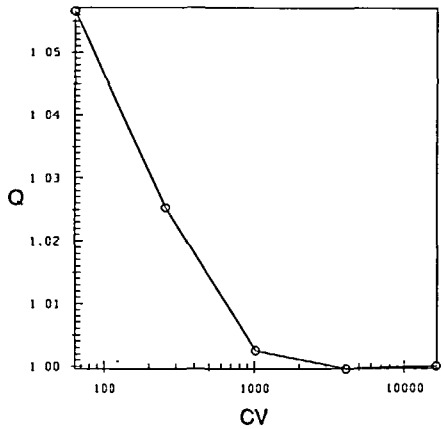

Figure 5 Variation of the normalized heat flux Q as a function of grid fineness

Table 4 Parameters and results of calculations for the horizontal and vertical MOCVD reactors

Parameters		Horizontal reactor	Vertical reactor
Finest grid (levels)		160×64 CV (5)	288×80 CV (5)
Error of the view factor calculations	e_C	1.29×10^{-2}	2.78×10^{-2}
	e_L	8.52×10^{-5}	1.19×10^{-4}
Re		8.21	14.6
Ra		3.36×10^{4}	5.56×10^{4}
Rad		11.8	23.1
Res_n/Res_0		10^{-6}	10^{-7}
Calculation time (min)		84	175
$Time_{SG}/Time_{MG}$		5.4	46.0

Flow and heat transfer effects play a critical role in MOCVD reactors and can be satisfactorily predicted only by taking into account the detailed boundary conditions including the processes of heat conduction in the reactor walls, external and internal radiation in the reactor chamber, external radiation and natural or forced convective heat transfer to the ambient. In order to demonstrate the ability of the present method to analyze complex problems, the flow and heat transfer were studied for horizontal and vertical reactor configurations. These problems include blocking surface, various types of obstacles in the solution domain as well as heat sources and buoyancy-driven flow.

The sets of parameters for both cases are collected in *Table 4*. The view factors for the vertical geometry were calculated with $N_\theta = 80$, $N_{sub} = 2$ and the correction technique was used. Accurate modelling of such flows needs a more realistic description of the radiative properties of the walls and hot zones, as they may differ significantly and may be the wavelength dependent like transmittance in the case of the quartz glass[10–12]. The aim of this study is to demonstrate the possibility of the efficient and numerically accurate calculation of combined flow and heat transfer processes in complex geometries including radiation, so no effort has been made to evaluate the modelling errors due to the limitations of assumptions used here when compared to real conditions in an experiment.

Results of calculations for the horizontal reactor are shown in *Figures 6* and *7*. In one case (*Figure 6*) radiation was ignored and the walls are assumed to be adiabatic, except for the heated

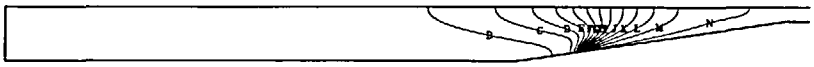

Figure 6 Above: Isotherms for the horizontal reactor—adiabatic boundary conditions; contour levels from 950 K (N) to 350 K (B), in steps of 50 K.
Below: Streamlines for the horizontal reactor—adiabatic boundary conditions. $\Psi_{max} = 1.09 \times 10^{-4}$ (O), $\Psi_{inflow} = 7.39 \times 10^{-5}$

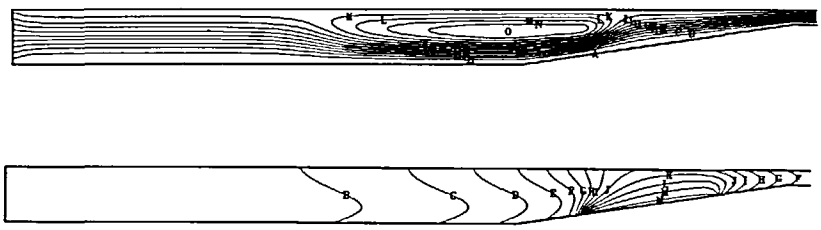

Figure 7 Above: Isotherms for the horizontal reactor—radiative boundary conditions; contour levels from 950 K (N) to 350 K (B), in steps of 50 K.
Below: Streamlines for the horizintal reactor—radiative boundary conditions. $\Psi_{max} = 9.51 \times 10^{-5}$ (O), $\Psi_{inflow} = 7.39 \times 10^{-5}$

section of the inclined lower wall (at the susceptor), which is kept at a constant temperature. In the other case (*Figure 7*), radiation is taken into account as described above. Obviously, there is a big difference in flow and temperature distributions for the two conditions. In both cases a high numerical accuracy was assured by using fine numerical grids (160 × 64 CV). Discretization errors were estimated by comparison of solutions on successive grids[14] and were found to be of the order of 0.03% on the finest grid. The radiation heat transfer causes the recirculation region at the upper wall to extend almost up to the inlet plane (where a uniform block velocity profile was specified in both cases).

The vertical reactor represent an axi-symmetric geometry with a submerged disc-shaped obstacle (the heated susceptors and suceptor holder), cf. *Figures 8* and *9*. The gas enters the pipe at the top and flows around the obstacle, leaving through the exhaust at the bottom. Both the susceptor and the centrally located holder are held at a constant temperature. In one case all other walls were considered adiabatic (*Figure 8*), in the other radiative boundary conditions were assumed on all boundaries (*Figure 9*). Calculations were performed on five grids, the finest having 288 × 80 CV. Discretization errors were estimated by comparing the solutions on consecutive grids and were found to be of the order of 1% on the finest grid in both cases. Computing time using multigrid solver and comparison with the single grid version are indicated in *Table 4*.

In the case of adiabatic boundary conditions and no radiation, buoyancy forces let gas above the susceptor flow upwards along symmetry axis like a plume. This upcoming flow is turned back by the incoming gas at the inlet boundary, where a block velocity profile was specified. Thus a large recirculation region is formed, which extends also behind the susceptor; the incoming gas flows along the outer wall.

In the case of radiative boundary conditions, completely different flow and temperature distribution were obtained, cf. *Figure 9*. The oncoming gas flows along the symmetry axis, impinges onto the susceptor, flows then radially and separates at the outer disk edge. Another large recirculation region is now attached to the outer wall.

Similar flow patterns and the effect of radiation in vertical reactors were also reported by

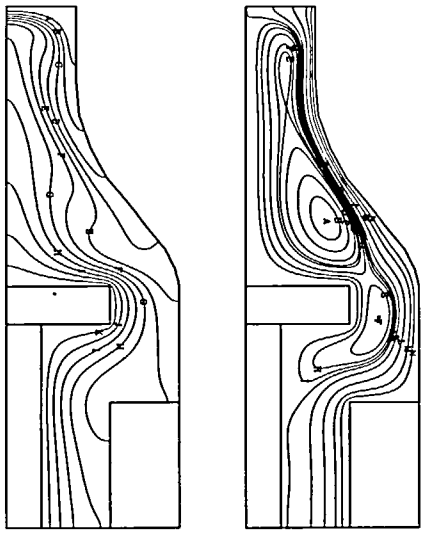

Figure 8 Left: Isotherms for the vertical reactor—adiabatic boundary conditions; contour levels from 850 K (K) to 250 K (A), in steps of 50 K.
Right: Streamlines for the vertical reactor—adiabatic boundary conditions. $\Psi_{min} = -9.33 \times 10^{-6}$ (A), $\Psi_{inflow} = 6.55 \times 10^{-6}$

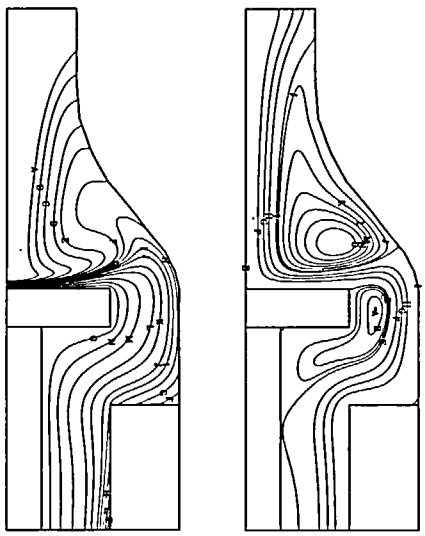

Figure 9 Left: Isotherms for the vertical reactor—radiative boundary conditions. Contour levels (O)—850 K, to (L) 700 K, in steps of 50 K; (K)—675 K, (J)—650 K, to (F)—600 K, in steps of 12.5 K; (E)—575 K, (D)—550 K, to (A)—400 K, in steps of 50 K.
Right: Streamlines for the vertical reactor—radiative boundary conditions. $\Psi_{max} = 1.41 \times 10^{-5}$, $\Psi_{inflow} = 6.55 \times 10^{-6}$

Fotiadis *et al.*[9]. The detailed study of transport processes in MOCVD reactors including the complex heat transfer and real material properties is the aim of the forthcoming studies.

The main aim of the present calculations was to demonstrate the efficiency of the present multigrid solution method when calculating flows in complex geometries with radiative boundary conditions. Solutions on five grids (the finest with 288×80 CV) on a workstation SUN SPARC

1+ were obtained in 175 minutes. It should be noted that for practical applications a less stringent convergence criterion can be used (iterative convergence error of the order of 0.1% instead of 0.001% used here), which would result in much shorter computing times.

CONCLUSION

In this paper, a 2D mathematical model for grey-diffusive surface radiation combined with the transport equations for mass, momentum and heat was presented. The mathematical model was implemented in a solution procedure for 2D (plane and axi-symmetric) laminar flows. The algorithm for the calculation of view factors provided the needed accuracy for the complex geometries. Through the use of the multigrid algorithm, high numerical efficiency was achieved. By using a sequence of systematically refined grids, it was possible to estimate the discretization errors in the numerical solutions. In examples considered here the discretization error on the finest grids were of the order of or below 1%.

The introduction of the multigrid technique has resulted in an efficient method for solving realistic problems involving grey-body radiation exchange, such as flow and radiation heat transfer in MOCVD reactors. This model and the implemented numerical technique could serve as a basis for computer-implemented process optimization and control strategies.

Concerning the future developments of the method, several new features will be included, like higher-order integration technique and using Stokes' theorem for view factor calculations and parallel processing using blockstructured grids and domain decomposition technique. For MOCVD applications, the complex heat transfer and real material properties as well as chemical reactions and species transport must be considered. This work is under way[15].

ACKNOWLEDGMENTS

The authors are grateful to F. Durst and M. Schäfer for valuable discussions and comments. The work in the present paper received financial support through the "Bavarian Consortium for High Performance Scientific Computing". This support is thankfully acknowledged.

The numerical method and the basic computer code used in these predictions were developed within the DFG-special progammes "Finite Approximationen der Strömungsmechanik" and "Strömungssimulation mit Hochleistungsrechnern".

REFERENCES

1 Howell, J. R. Thermal radiation in participating media: the past, the present and some possible futures, *Trans. ASME*, **110**, 1220–1229 (1988)
2 Siegel, R. and Howell, J. R. *Thermal radiation heat transfer*, McGraw-Hill, New York (1981)
3 Sparrow, E. M. and Cess, R. D. *Radiation heat transfer*, McGraw-Hill, New York (1978)
4 Bornside, D. E., Kinney, T. A., Brown, R. A. and Kim, G. Finite element/newton method for the analysis of Czochralski crystal growth with diffuse-grey radiative heat transfer, *Int. J. Num. Meth. Eng.*, **30**, 133–154 (1990)
5 Atherton, L. J., Derby, J. J. and Brown, R. A. Radiative heat exchange in Czochralski crystal growth, *J. Cryst. Growth*, **84**, 57–78 (1987)
6 Dupret, F., Nicodeme, P., Ryckmans, Y., Wouters, P. and Crochet, M. J. Global modelling of heat transfer in crystal growth furnaces, *Int. J. Heat Mass Transfers*, **33**, 1849–1871 (1990)
7 Dupret, F., Nicodeme, P. and Ryckmans, Y. Numerical method for reducing stress level in GaAs crystals, *J. Cryst. Growth*, **97**, 162–172 (1989)
8 Dupret, F., Ryckmans, Y., Wouters, P. and Crochet, M. J. Numerical calculation of the global heat transfer in a Czochralski furnace, *J. Cryst. Growth*, **79**, 84–91 (1986).
9 Fotiadis, D. F., Kieda, S. and Jensen, K. F. Transport phenomena in vertical reactors for metalorganic vapor phase epitaxy, *J. Crystal Growth*, **102**, 441–470 (1990)
10 Fotiadis, D. F., Boekholt, M., Jensen, K. F. and Richter, W. Flow and heat transfer in CVD reactors: comparison of Raman temperature measurements and finite element model predictions, *J. Crystal Growth*, **100**, 577–599 (1990)
11 Kleijn, C. R. and Hoogendoorn, C. J. A study of 2- and 3-D transport phenomena in horizontal chemical vapor deposition reactors, *Chemical Eng. Sci.*, **46**, 321–334 (1991)

12 Chinoy, P. B., Kaminiski, D. A. and Ghandhi, S. K. Effects of thermal radiation on momentum, heat, and mass transfer in a horizontal chemical vapor deposition reactor, *Num. Heat Transfer*, Part A, **19**, 85–100 (1991)
13 Field, R. J. Simulations of two-dimensional recirculating flow effects in horizontal MOVPE, *J. Crystal Growth*, **97**, 739–760 (1989)
14 Hortmann, M., Perić, M. and Scheuerer, G. Finite volume multigrid prediction of laminar natural convection: bench-mark solutions, *Int. J. Num. Meth. Fluids*, **11**, 189–207 (1990)
15 Durst, F., Kadinskii, L., Perić, M. and Schäfer, M. Numerical study of transport phenomena in MOCVD reactors using a finite volume multigrid solver, *J. Crystal Growth*, **125**, 612–626 (1993)
16 Engelman, M. and Jamnia, M.-A. Grey-body surface radiation coupled with conduction and convection for general geometries, *Int. J. Num. Meth. Fluids*, **13**, 1029–1053 (1991)
17 Demirdžić, I, and Perić, M. Finite volume method for prediction of fluid flow in arbitrarily shaped domains with moving boundaries, *Int. J. Num. Meth. Fluids*, **10**, 771–790 (1990)
18 Patankar, S. V. and Spalding, D. B. A calculation procedure for heat, mass and momentum transfer in three-dimensional parabolic flows, *Int. J. Heat Mass Transfer*, **15**, 1787–1806 (1972)
19 Stone, H. L. Iterative solution of implicit approximations of multi-dimensional partial differential equations, *SIAM J. Num. Anal.*, **5**, 530–558 (1968)
20 Perić, M., Rüger, M. and Scheurer, G. Finite-volume multigrid method for calculating turbulent flows, *Proc. 7th Symp. on Turbulent Shear Flows*, Stanford, CA, 7.3.1–7.3.6 (1989)
21 Demirdžić, I., Lilek, Ž. and Perić, M. Fluid flow and heat transfer test problems for non-orthogonal grids: bench-mark solutions, *Int. J. Num. Meth. Fluids*, **15**, 329–354 (1992)
22 Howell, J. R. *A catalog of radiation configuration factors*, McGraw-Hill, New York (1982)